Size and composition-controlled fabrication of VO_2 nanocrystals by terminated cluster growth

By *César Clavero*, Jonathan Slack* and *André Anders*

Lawrence Berkeley National Laboratory
1 Cyclotron road, Berkeley, California, 94720 (USA)
E-mail: cclavero@lbl.gov

Keywords: terminated cluster growth, thermochromism, plasmonics, nanoparticles.

A physical vapor deposition-based route for the fabrication of VO_2 nanoparticles is demonstrated, consisting of reactive sputtering and vapor condensation at elevated pressures. The oxidation of vanadium atoms is an efficient heterogeneous nucleation method, leading to high nanoparticle throughtput. Fine control of the nanoparticle size and composition is obtained. Post growth annealing leads to crystalline VO_2 nanoparticles with optimum thermocromic and plasmonic properties.

Keywords: terminated cluster growth, thermochromism, plasmonics, nanoparticles

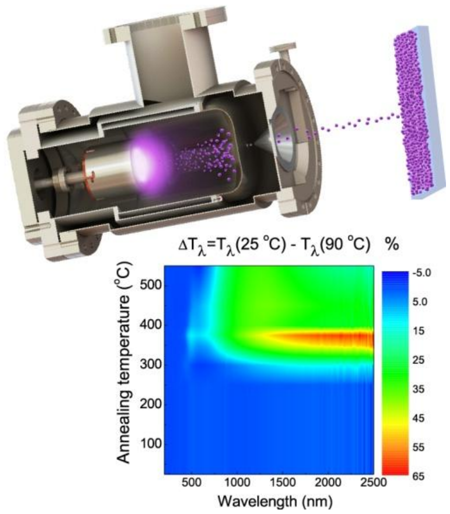

Metals and semiconductor nanoparticles are increasingly attracting the attention of researchers from a broad spectrum of disciplines due to their unprecedented physical and chemical properties. Nanoparticles have multiple interesting applications in sensors,[1] catalysis[2] and even cancer treatment.[3] In addition, metal, semiconductor and conducting oxide nanoparticles are interesting due to their outstanding plasmonic properties. They allow efficient light trapping in photovoltaic[4] and photocatalysis devices,[5] and active tuning of the transmittance in smart windows.[6] For all the mentioned applications, an accurate control of nanoparticle size, composition and crystallinity is critical to obtain the desired properties.

Vanadium dioxide is a material of especial interest due to its thermochromic and plasmonic properties. It exhibits a semiconductor to metal (MIT) transition at around 68 °C that is accompanied by a first order structural phase transition from monoclinic to rutile. As a consequence, a drop in the resistance of around four orders of magnitude is observed,[7] resulting in a remarkable increase in IR reflectance and a corresponding decrease in transmittance.[8] The origin of this transition still remains controversial. It is unclear whether the insulating behavior in the low temperature phase is due to a Peierls distortion inducing the insulator energy gap, or to a Mott transition due to electron localization and increase in electron-electron repulsion.[9] In addition, VO_2 nanoparticles composites, which are the scope of this work, have different thermochromic properties than continuous thin films. They exhibit a superior modulation of the transmittance in the visible and near IR portion of the spectrum due to plasmonic effects when the nanoparticles are in their metallic state[10]. This offers new opportunities for applications such as smart windows.

While fabrication of VO_2 thin films has been extensively investigated in the last decades, very few studies have focused on the fabrication of nanoparticles. Gea *et al.*[11] obtained VO_2 nanoparticles by stoichiometric co-implantation of V and O atoms on sapphire and subsequent annealing at temperatures ranging from 700 to 1000 °C. In a similar approach, Lopez *et al.*[12] obtained VO_2 nanorods by implantation and annealing at a high temperature of

1000 °C. Using this technique they were able to investigate the effect of Ti and W doping. Other authors have reported the fabrication of VO_2 nanocomposites using magnetron sputtering co-deposition.[13] Also, a variety of chemical methods have been used including sol-gel, inverse miscelle, arrested precipitation and aerosol process. Common to the various methods and motivations for producing VO_2 nanoparticles previously mentioned is the lack of a reliable method to selectively control composition, size, and the degree of crystallinity.

Here, a physical vapor deposition-based route is demonstrated for the fabrication of VO_2 nanoparticles. This technique, also known as terminated cluster growth (TCG), is based on the condensation of an atomic vapor produced by magnetron sputtering at relatively high pressure.[14, 15] The supersaturated vapor cools down due to frequent collisions with inert gas atoms, which leads to condensation and formation of clusters and nanoparticles. The classical nucleation theory can be used to describe the homogeneous nucleation and growth of nanoparticles in the aggregation zone.[16, 17] According to this formalism, the change in free energy ΔG associated with the aggregation of n atoms from the metal vapor into a nanoparticle is given by the energy spent forming the nanoparticle surface and the chemical potential variation $\Delta\mu$ during vapor condensation. A maximum in ΔG and thus optimum condensation conditions are achieved in a narrow area of the aggregation zone where the temperature of the gas phase, *i.e.* metal vapor plus inert gas mixture, favors nucleation.[17] Under these circumstances, the formation of embryos takes place following a three body collision process between two sputtered atoms and one Ar atom.[18] After nucleation, nanoparticle growth takes place by successive two body collisions between the nanoparticles and the individual atoms in the metal vapor, or by coagulation, *i.e.* inelastic particle-particle collisions.[15]

However, heterogeneous nucleation occurs much more often in nature, as it requires a lower variation in free energy. It takes place in preferential sites such as phase boundaries, contaminants, ions, surfaces or it is triggered by chemical reactions.[15, 16] Creation of oxide nanoparticles from gas condensation of a metal vapor in the presence of oxygen is a prominent example of heterogeneous nucleation.[15] In this case, a chemical reaction, *i.e.* oxidation of the metal atoms, is the first step in the nanoparticle formation process. Marek *et al.*[19] observed an abrupt increase in the Cu and Ti nanoparticle formation when adding marginal amounts of oxygen at a flow of around 0.05 sccm. Similar observations were reported by Peter *et al.*[20] for Ti and Co nanoparticles in the presence of oxygen and nitrogen respectively. Other authors used this method to create nanoparticle oxides such as ZnO[21] or TiO_2.[22]

In this work, we present a comprehensive study on the fabrication of crystalline VO_2 nanoparticles by TCG and subsequent annealing treatments. The nanoparticle nucleation and growth processes were investigated as a function of the relative flow rates of Ar and O_2. The composition, morphology and crystal structure of the fabricated nanoparticles are characterized following a multi-technique approach. Special attention is given to their spectral optical response to temperature changes and switching characteristics.

In a first step, experiments were carried out keeping the Ar flow rate constant and varying the oxygen flow.

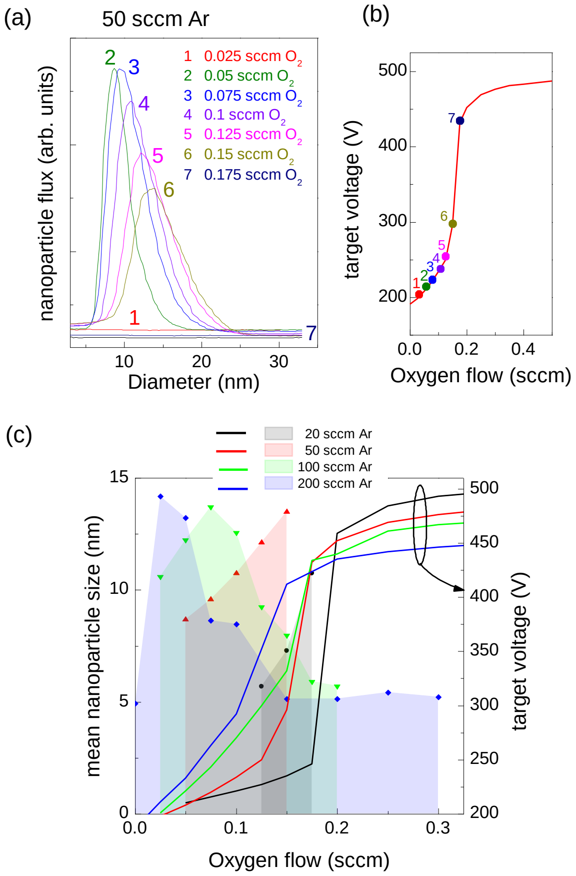

Figure 1 (a) shows the nanoparticle size distribution measured by the linear quadrupole mass spectrometer for an Ar flow of 50 sccm (corresponding to 290 mTorr in the aggregation zone) and oxygen flows ranging from 0 to 0.175 sccm. No nanoparticle production is registered for oxygen flows below 0.025 sccm. This fact is due to the inability of the metal vapor to cool down and condensate through homogeneous nucleation at such a low inert gas pressure. Higher Ar flow rates starting at 100 sccm are needed for this purpose. However, an abrupt increase in the nanoparticle production is observed when just 0.05 sccm of oxygen are added to the aggregation zone. This illustrates the increased efficiency of the

heterogeneous embryo formation mechanism in this system. The nanoparticle size distribution curves shown in Figure **1** (a) exhibit a characteristic Gaussian curve shape,[17] centered at the mean nanoparticle diameter. A bulk VO_2 density value (4.6 g cm^{-3}) was considered to calculate the nanoparticle diameter from the mass values measured by the quadrupole mass spectrometer.

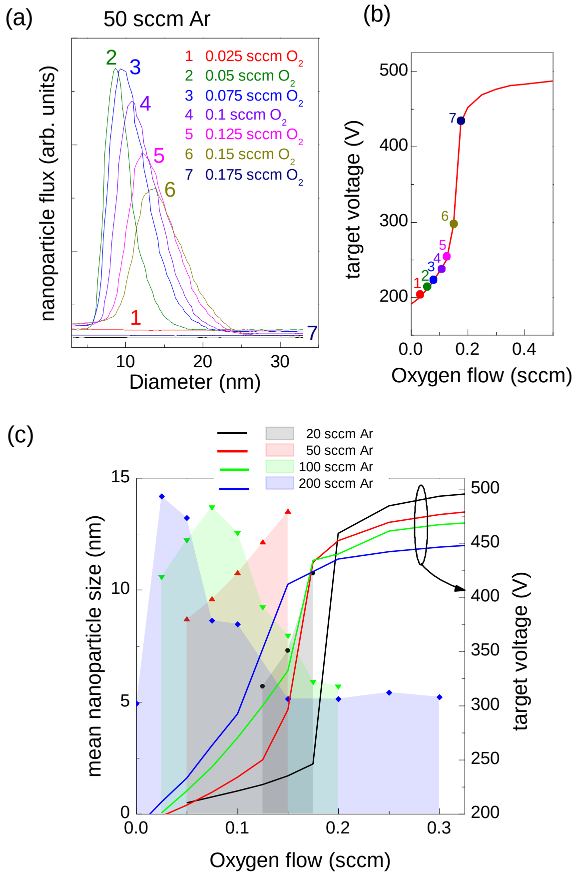

Increasing nanoparticle sizes are obtained as the flow of O_2 increases, ranging from 5 to 25 nm.

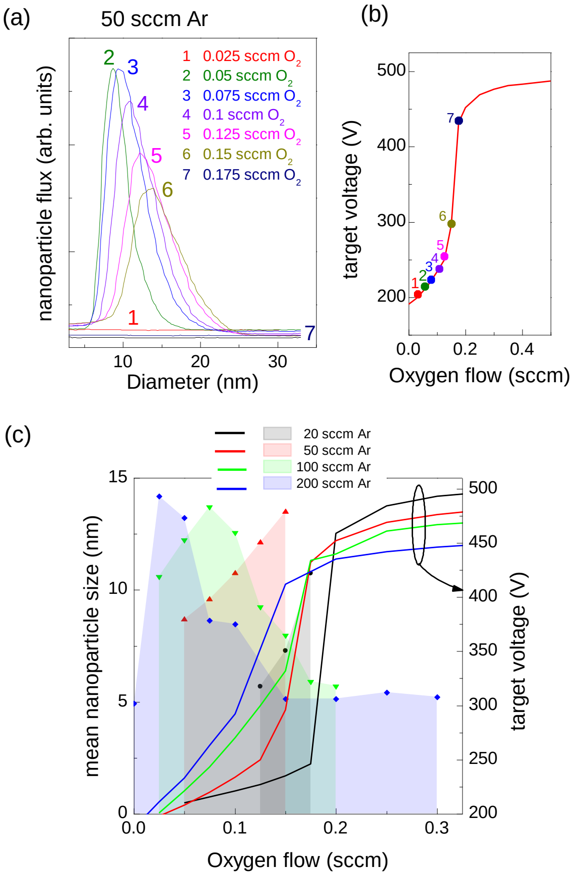

Figure **1** (b) shows the target voltage as a function of oxygen flow, an important parameter when performing reactive sputtering. Poisoning of the target takes place starting at very low O_2 flow rates, with a 0.2 sccm rate driving the system fully into de oxide cathode state. The production of nanoparticles ends at this point. The mean nanoparticle size and target voltage were also investigated for Ar flow rates from 20 to 200 sccm, which corresponds to pressures in the aggregation zone from 120 to 1050 mTorr.

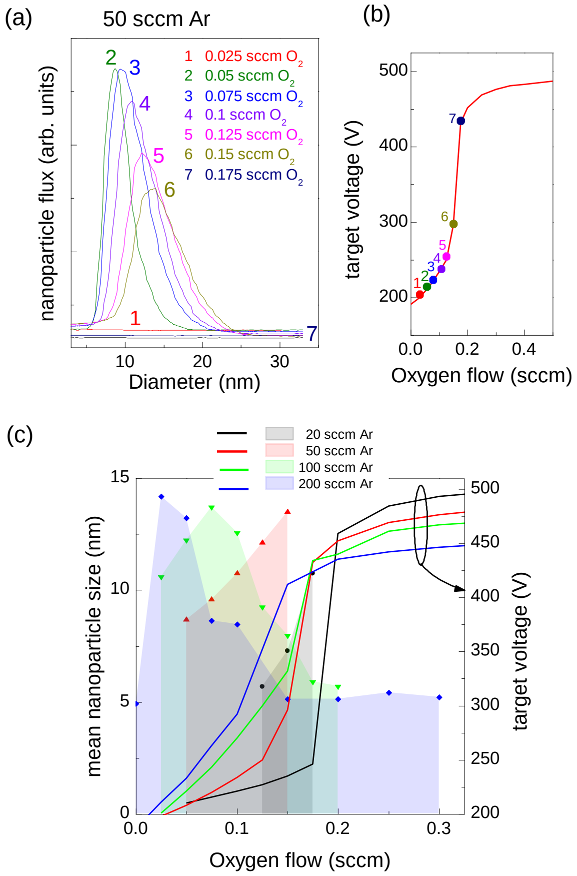

Figure **1** (c) depicts the dependence of the mean nanoparticle size (left axis) and target voltage (right axis) on the oxygen flow rate. Again, the production of nanoparticles is restricted to a very narrow window of oxygen flow rates in most of the cases. Nanoparticles are produced over a broader range of O_2 flows as the Ar flow rate is increased. Interestingly, nanoparticle formation is detected by the quadrupole mass spectrometer for 200 sccm Ar flow rate even when the target is in the oxide state. However the growth rate was below the detection limit (0.01 nm/s) of the crystal monitor in this range.

The composition, morphology and crystal structure of the prepared VO_2 nanoparticles was characterized by several complementary methods. The composition of the as-grown nanoparticle films was investigated using Rutherford backscattering spectroscopy (RBS). Figure 2 (a) shows the RBS spectrum and data fittings for a sample prepared at a pressure of 350 mTorr in the aggregation zone (corresponding to Ar and O_2 flow rates of 50 and 0.2 sccm, respectively) and 300 mA ion current at the target. The depth profiles for V and O clearly show stoichiometric VO_2 through the whole thickness of the film. Interestingly, samples grown at higher pressures show a different composition. Figure 2 (b) shows a RBS spectrum for a sample prepared with a pressure of 1 Torr in the aggregation zone (corresponding to Ar and O_2 flow rates of 200 and 0.2 sccm, respectively). The depth profiles obtained from the analysis of the spectrum correspond to a composition close to VO through the whole film. This change in composition can be ascribed to the considerably higher carrier gas flow rate in the latter case. The higher Ar partial pressure in the aggregation zone promotes homogeneous nucleation and growth, hence lessens the fraction of oxygen incorporated in the nanoparticles.

Even though the nanoparticles prepared at a pressure of 350 mTorr in the aggregation zone were found to have the desired VO_2 stoichiometry, they were found to be amorphous, as evident by x-ray diffraction (XRD). It is well known that while other V oxides such as V_2O_5 and V_2O_3 are very stable, VO_2 is a metastable oxide that can be formed under specific chemical environments and thermal conditions. Post growth thermal annealing at temperatures ranging from 100 to 650 °C was carried out in a furnace for 30 minutes under Ar atmosphere.

The morphology of the as-deposited and annealed nanoparticles was investigated using scanning electron microscopy (SEM). For this characterization technique, glassy carbon substrates were selected to avoid charging effects. The same deposition conditions used in the sample shown in Figure 2 (a) were used. For this series of samples, the nanoparticles had an average diameter of 8 nm as measured by the linear quadrupole mass spectrometer considering bulk VO_2 density. However, the as-deposited nanoparticles exhibit an average size of 10 nm in the SEM image (Figure 3). A considerable growth in average size is observed after annealing due to temperature-activated Oswald ripening and aggregation. Nanoparticles of around 25 nm are observed when annealing at 375 °C for 30 minutes in Ar.

The crystal structure of the nanoparticle films was investigated as a function of the annealing temperature using XRD. The samples annealed at temperatures lower than 550 °C were deposited on glass, though the sample annealed at 650 °C was deposited on glassy carbon to avoid softening of the glass substrate. Figure 4 shows the obtained 2theta spectra. No crystal structure is detected until annealing temperatures reached around 300 °C, where hints of crystalline VO_2 are detected. Increasingly intense reflections are obtained for higher annealing temperatures. A combination of V_2O_5 and V_3O_7 phases is observed for the highest annealing temperature of 650 °C. The crystal grain size of the VO_2 phase was calculated from the width of the VO_2 (011) reflections using the Scherrer equation,[23] as shown in Figure 4 (b). A progressive increase in crystallite size is observed, starting at 10.6 nm when annealing at 350 °C and increasing up to 18.2 nm at 550 °C. This increase in size is in tune with the SEM observations described in Figure 3.

The spectral optical response to a change in temperature was investigated as a function of the annealing temperature, both in the low temperature semiconductor and the high temperature metallic states of VO_2. Figure 5 (a) shows the transmittance T_λ spectra for as-deposited nanoparticle films and annealed at different temperatures ranging from 250 to 550 °C. The transmittance spectra measured at room temperature are shown on the left and those measured at 90 °C are depicted on the right. While the samples annealed at temperatures lower than 375 °C have a high infrared transmittance in their semiconducting state, a considerable drop of up to 40 % takes place when annealed at higher temperatures. Significant switching of the infrared transmittance is observed for samples that were annealed at temperatures starting at 300 °C and measured at an elevated temperature of 90 °C [Figure 5 (b) right]. To better illustrate the spectral switching mechanism, Figure 5 (b) depicts a map of the variation in transmittance between the semiconductor and metallic states $\Delta T_\lambda = T_\lambda$ (25 °C) - T_λ (90 °C) as a function of the annealing temperature and incident light wavelength. Maximum transmittance variation is obtained in a narrow annealing temperature region centered at 375 °C. The transmittance of the films, and the change observed upon heating, depends strongly on the thickness of the films. Higher transmittance values across the whole spectrum can be obtained by depositing thinner VO_2 nanoparticle films.

The switching characteristics of the different nanoparticle films were investigated by registering their transmittance during the warming up and cooling down processes. Figure 6 (a) shows the hysteresis loops obtained for some selected samples. While no significant switching takes place for the unannealed sample and those annealed at temperatures lower than 250 °C (ΔT_{λ} around 1.8 % maximum), a broad hysteresis is obtained for samples annealed at higher temperatures. Optical switching takes place at 71.2 °C for the sample annealed at 375 °C, calculated as the point with maximum negative slope in the loop. The large hysteresis of these samples, of around 30 °C, is directly related to their nanoparticle microstructure, which favors a broad dispersion of switching temperatures. This contrasts with the narrow hysteresis breadths found in VO_2 continuous thin films.[24] The loop reported by Verleur *et al.*[24] for a continuous thin film is shown in Figure 6 (b) for comparison. As the annealing temperature is increased, even broader hysteresis loops of up to 36 °C are obtained. Figure 6 (b) shows transmittance T_{λ} maps as a function of annealing temperature with the sample warming up (top) and cooling down (bottom). Interestingly, while no large variations are observed in the switching temperature for samples annealed at 350 °C and higher while warming up, a progressive decrease of the switching temperature as the annealing temperature increases is observed when cooling down.

In conclusion, VO_2 nanoparticle fabrication was demonstrated using terminated cluster growth with discrete process parameter control over their composition, size and crystallinity. The reactive sputtering mechanisms combined with oxygen-induced heterogeneous nucleation proved to be an efficient heterogenous nanoparticle embryo formation mechanism leading to a high throughput (compared to homogenous cluster nucleation and growth). Control of the nanoparticle composition and size was demonstrated by tuning the growth conditions such as the partial pressures of carrier and reactive gases in the nucleation zone. Crystallization of the as-deposited oxide nanoparticles was achieved by thermal treatment. Maximum optical switching in the infrared was obtained for VO_2 nanoparticles annealed at 375 °C, with a transition temperature around 71 °C.

Experimental

VO_2 nanoparticles were fabricated using a Nanogen 50 nanoparticle deposition system from Mantis Deposition, Ltd. The source was installed in a vacuum chamber with base pressure in the low 10^{-7} Torr. The nanoparticle source consists of a 2 inch DC magnetron sputtering gun housed in a cavity known as the aggregation zone. After sputtering of the V target at an elevated pressure of Ar (typically between 20 and 1000 mTorr), condensation of the metal vapor takes place giving rise to the formation of nanoparticles. In addition, introduction of relatively small concentrations of oxygen in the aggregation zone gives rise to considerably more efficient heterogeneous nucleation and the formation of VO_2 nanoparticles. Multiple factors can be modified during the fabrication process, the most important ones being ion current to the target, target position within the aggregation zone and carrier gas flow rate.[17] After formation, the nanoparticles leave the aggregation zone through a 3 mm diameter aperture aligned axially with the sputtering gun and are accelerated toward the main chamber thanks to the pressure difference between the aggregation zone and the main chamber. Most of the nanoparticles acquire a single negative charge during the nanoparticle formation process[17], which allows mass selection by means of a linear quadrupole mass spectrometer (MesoQ from Mantis Deposition Ltd). A quartz crystal monitor was used to measure the nanoparticle deposition rates. In this study, an aggregation zone length of 130 mm and an ion current to the target of 300 mA were used. The oxygen and argon flow rates were varied in order to tune the size and composition of the nanoparticles.

Borosilicate microscope glass slides and glassy carbon substrates were used as substrates. The glass slides were cleaned with Liquinox, a widely used glass detergent containing ethylene diamine tetra acetate, designed to yield completely residue-free surfaces. After being rinsed with ultra pure water and quickly dried using dry Ar, they were ultrasound cleaned in an isopropyl alcohol bath. In the case of the glassy carbon substrates only the latter cleaning treatment was applied. Post growth treatment was carried out *ex situ* in an oven at temperatures ranging from 100 to 650 °C in Ar atmosphere to achieve crystallization of the as-deposited nanoparticles.

The morphology of the nanoparticles was investigated using scanning electron microscopy (SEM) in an Ultra 55 FESEM instrument. The chemical composition and structure was investigated using Rutherford backscattering spectroscopy (RBS). This technique detects the energies and amount of backscattered He ions from a solid target, and can be used to quantitatively investigate the depth profile of individual elements in a solid. The measurements were carried out using a model 5SDH Pelletron tandem accelerator manufactured by National Electrostatics Corporation (NEC). The crystal structure was investigated using a Bruker AXS D8 Discover GADDS x-ray diffractometer (XRD) equipped with a HighStar area detector and operated at the Cu K_α wavelength (1.54 Å).

Optical measurements were carried out using a Perkin Elmer Lambda 19 spectrophotometer in the spectral range from 220 to 2500 nm. The instrument was retrofitted with a variable temperature sample stage in order to register the temperature dependence of the transmittance.

Acknowledgements

This work was supported by the Assistant Secretary for Energy Efficiency and Renewable Energy, Office of Building Technology, of the US Department of Energy under Contract No.

DE-AC02-05CH11231. Work at the Molecular Foundry was supported by the Office of Science, Office of Basic Energy Sciences, of the U.S. Department of Energy under Contract No. DE-AC02-05CH11231.

Disclaimer

Figures

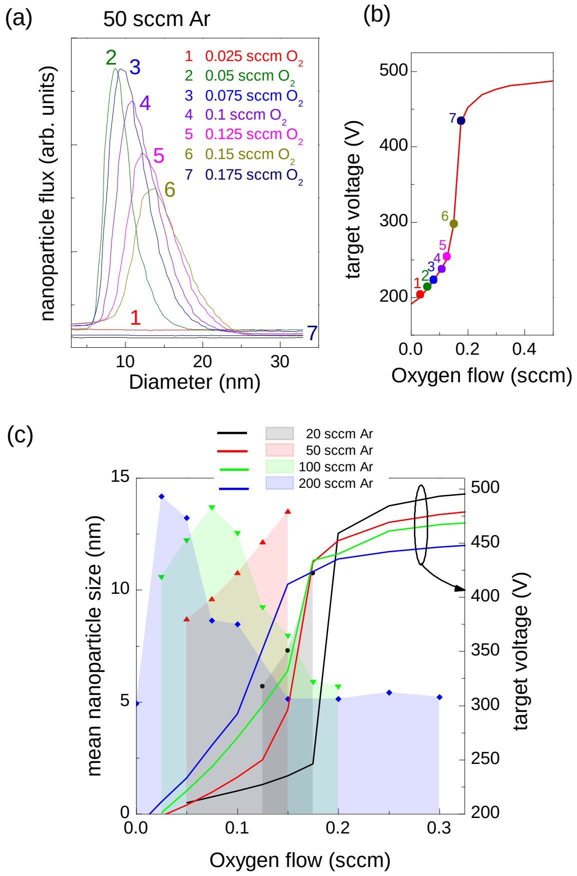

Figure 1. (a) Size distributions for nanoparticles fabricated with an Ar flow of 50 sccm and variable O_2 flows from 0 to 0.175 sccm. (b) Target voltage vs. oxygen flow. (c) Mean

nanoparticle size (left axis) and voltage in the target (right axis) vs. oxygen flow for nanoparticles deposited using Ar flows from 20 to 200 sccm (120 to 1050 mTorr in the aggregation zone).

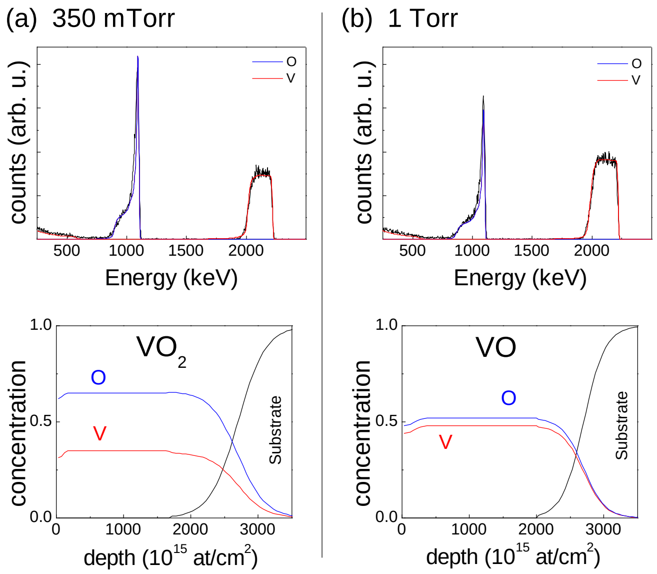

Figure 2. (a) Rutherford backscattering spectroscopy (RBS) scans (top) for a film consisting of nanoparticles grown at a pressure of 350 mTorr. The calculated concentration profile (bottom) shows VO_2 formation thorough the whole film. (b) RBS spectrum and concentration profile for nanoparticles grown at 1 Torr showing VO composition.

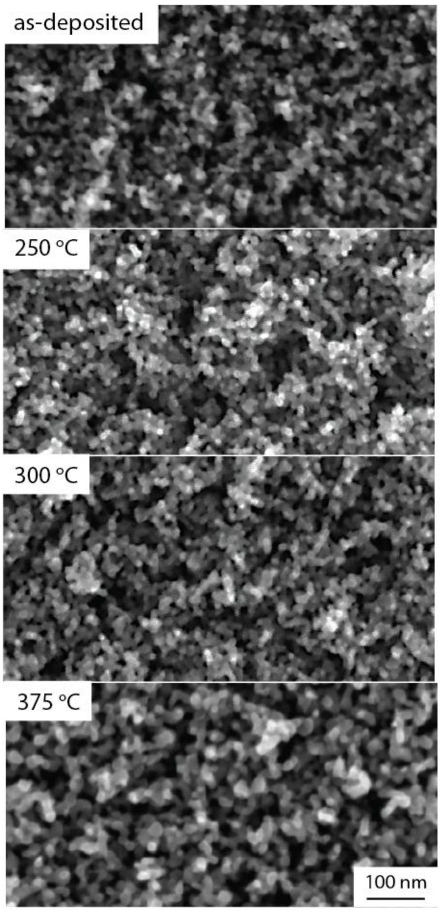

Figure 3. Scanning electron microscopy (SEM) images for the as-deposited VO_2 nanoparticles and after annealing at temperatures up to 375 °C for 30 minutes in argon.

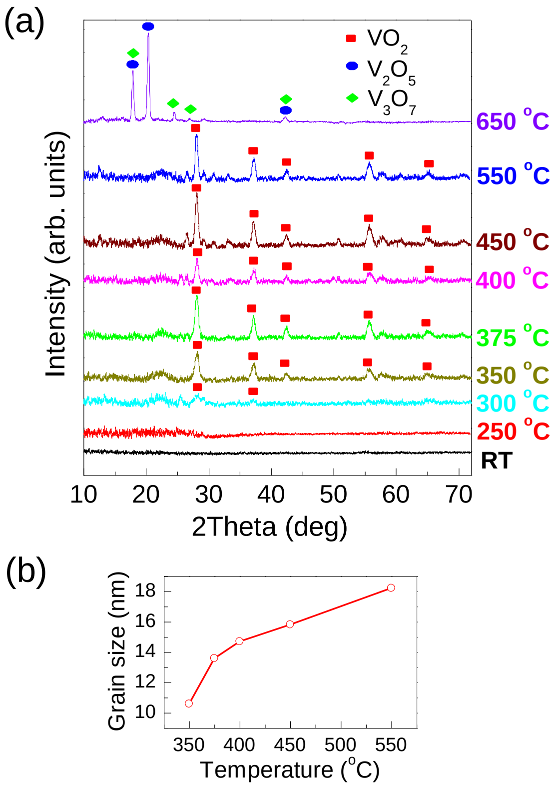

Figure 4. (a) X-ray diffraction scans for the nanoparticle films as-deposited and annealed at temperatures from 250 to 650 °C. (b) VO_2 grain size as a function of annealing temperature calculated using the VO_2 (011) reflection.

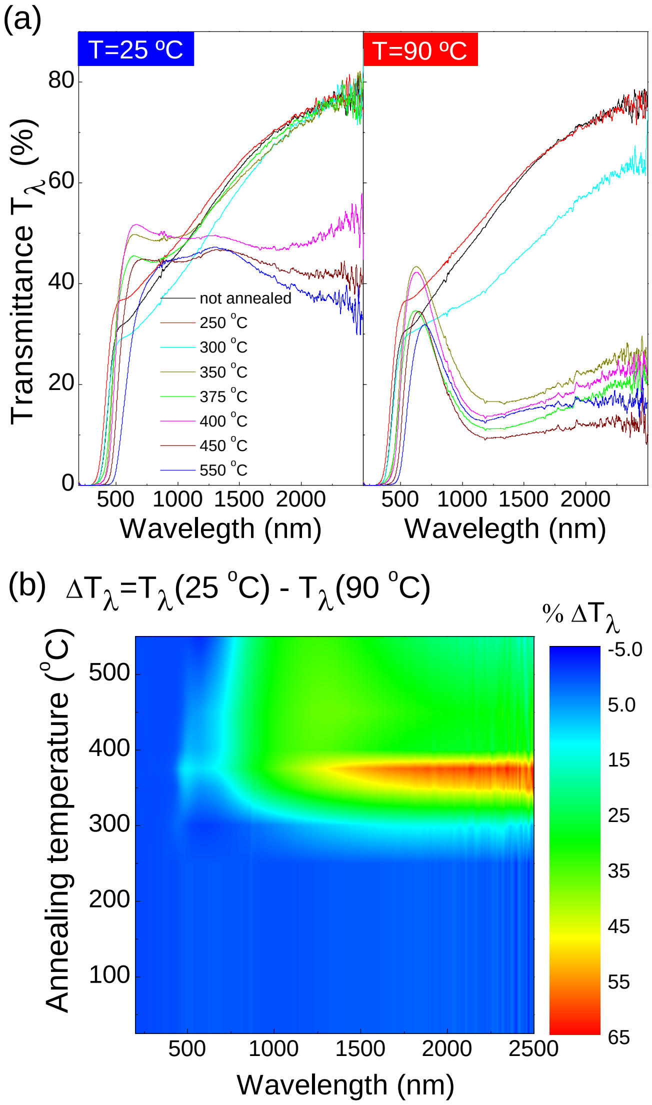

Figure 5. (a) Spectral transmittance for the nanoparticle films annealed at different temperatures measured at room temperature (left) and at 90 °C (right). (b) Map of the variation in transmittance between the semiconductor and metallic states $\Delta T_\lambda = T_\lambda$ (25 °C) - T_λ (90 °C) as a function of the annealing temperature and incident light wavelength.

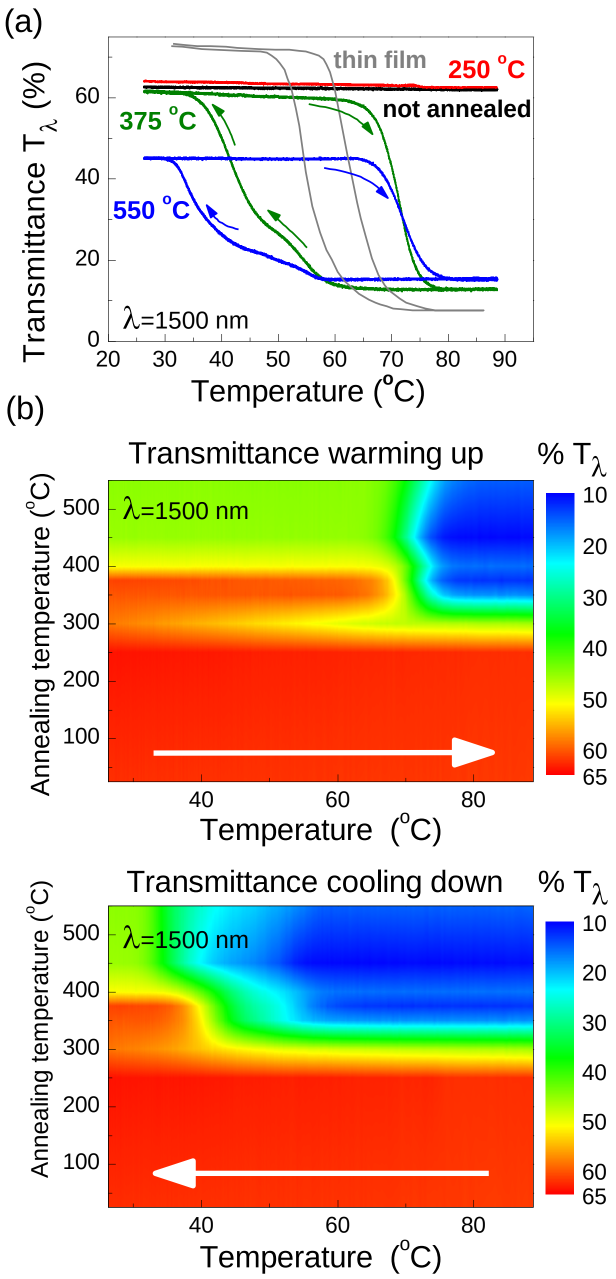

Figure 6. (a) Transmittance hysteresis loops for nanoparticle films annealed at different temperatures measured at λ=1500 nm. A loop conrresponding to a continuous thin film from ref. [24] is shown in grey for comparison. (b) Transmittance maps as a function of the annealing temperature and the sample temperature while warming up (top) and cooling down (bottom).

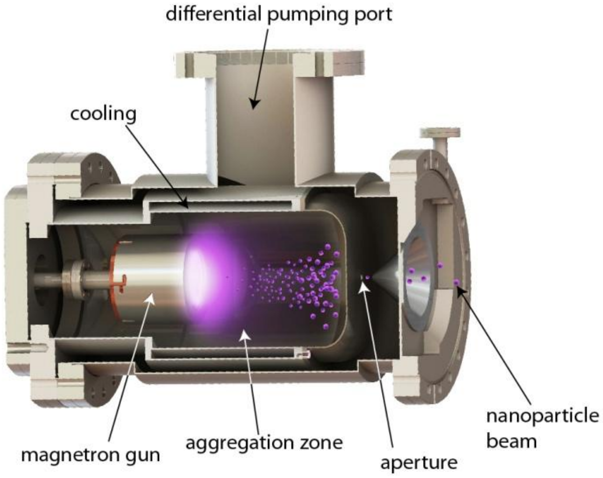

Figure 7. Terminated cluster growth source. A DC magnetron sputtering gun is housed in the aggregation zone, where the supersaturated vapor condensed in the form of nanoparticles. (Nanogen 50 by Mantis Deposition, Ltd.).

References

[1] A. G. Brolo, Nat Photon **2012**, 6, 709.
[2] A. Z. Moshfegh, Journal of Physics D: Applied Physics **2009**, 42, 233001.
[3] W. Brullot, V. K. Valev, T. Verbiest, Nanomedicine: Nanotechnology, Biology and Medicine **2012**, 8, 559.
[4] C.-Y. Fang, Y.-L. Liu, Y.-C. Lee, H.-L. Chen, D.-H. Wan, C.-C. Yu, Advanced Functional Materials **2012**, 23, 1412; S. Mokkapati, K. R. Catchpole, Journal of Applied Physics **2012**, 112, 101101.
[5] S. Linic, P. Christopher, D. B. Ingram, Nat Mater **2011**, 10, 911.
[6] G. Garcia, R. Buonsanti, E. L. Runnerstrom, R. J. Mendelsberg, A. Llordes, A. Anders, T. J. Richardson, D. J. Milliron, Nano Letters **2011**, 11, 4415.
[7] E. N. Fuls, D. H. Hensler, A. R. Ross, Applied Physics Letters **1967**, 10, 199.
[8] Z. Zhang, Y. Gao, Z. Chen, J. Du, C. Cao, L. Kang, H. Luo, Langmuir **2010**, 26, 10738.
[9] A. Cavalleri, T. Dekorsy, H. H. W. Chong, J. C. Kieffer, R. W. Schoenlein, Physical Review B **2004**, 70, 161102; M. Nakajima, N. Takubo, Z. Hiroi, Y. Ueda, T. Suemoto, Journal of Luminescence **2009**, 129, 1802; E. Sakai, K. Yoshimatsu, K. Shibuya, H. Kumigashira, E. Ikenaga, M. Kawasaki, Y. Tokura, M. Oshima, Physical Review B **2011**, 84, 195132.
[10] S. Y. Li, G. A. Niklasson, C. G. Granqvist, Journal of Applied Physics **2010**, 108, 063525; S.-Y. Li, G. A. Niklasson, C. G. Granqvist, Journal of Applied Physics **2011**, 109, 113515; S. Y. Li, G. A. Niklasson, C. G. Granqvist, Thin Solid Films **2012**, 520, 3823.
[11] L. A. Gea, L. A. Boatner, Applied Physics Letters **1996**, 68, 3081.
[12] R. Lopez, T. E. Haynes, L. A. Boatner, L. C. Feldman, J. R. F. Haglund, Opt. Lett. **2002**, 27, 1327; R. Lopez, L. A. Boatner, T. E. Haynes, L. C. Feldman, J. R. F. Haglund, Journal of Applied Physics **2002**, 92, 4031.
[13] A. Romanyuk, R. Steiner, L. Marot, V. Spassov, P. Oelhafen, Thin Solid Films **2008**, 516, 8513; J. B. Kana Kana, J. M. Ndjaka, B. D. Ngom, N. Manyala, O. Nemraoui, A. Y. Fasasi, R. Nemutudi, A. Gibaud, D. Knoesen, M. Maaza, Thin Solid Films **2010**, 518, 1641; M. Maaza, O. Nemraoui, C. Sella, A. C. Beye, B. Baruch-Barak, Optics Communications **2005**, 254, 188.
[14] C. Binns, Surface Science Reports **2001**, 44, 1.
[15] K. Wegner, P. Piseri, H. V. Tafreshi, P. Milani, Journal of Physics D: Applied Physics **2006**, 39, R439.
[16] W. Knauer, Journal of Applied Physics **1987**, 62, 841.
[17] E. Quesnel, E. Pauliac-Vaujour, V. Muffato, Journal of Applied Physics **2010**, 107, 054309.
[18] A. I. Ayesh, N. Qamhieh, H. Ghamlouche, S. Thaker, M. El-Shaer, Journal of Applied Physics **2010**, 107, 034317; T. Hihara, K. Sumiyama, Journal of Applied Physics **1998**, 84, 5270.
[19] A. Marek, J. Valter, S. Kadlec, J. Vyskočil, Surface and Coatings Technology **2011**, 205, Supplement 2, S573.
[20] T. Peter, O. Polonskyi, B. Gojdka, A. M. Ahadi, T. Strunskus, V. Zaporojtchenko, H. Biederman, F. Faupel, Journal of Applied Physics **2012**, 112, 114321.
[21] P. Thangadurai, I. Zergioti, S. Saranu, C. Chandrinou, Z. Yang, D. Tsoukalas, A. Kean, N. Boukos, Applied Surface Science **2011**, 257, 5366.
[22] S.-i. In, A. H. Kean, A. Orlov, M. S. Tikhov, R. M. Lambert, Energy & Environmental Science **2009**, 2, 1277.
[23] B. E. Warren, *X-Ray Diffraction*, Dover Publications, INC., New York **1990**.
[24] H. W. Verleur, A. S. Barker, C. N. Berglund, Physical Review **1968**, 172, 788.